Research Article

Jun Jin, Shan Jiang*, and Hongping Hu

# Multiple wide band gaps in a convex-like holey phononic crystal strip

https://doi.org/10.1515/rams-2022-0010
received October 14, 2021; accepted December 01, 2021

**Abstract:** A convex-like one-dimensional holey phononic crystal (PnC) strip with multiple wide band gaps but simple construction is investigated. By dint of the unique folding topology constituted by deformable L-shaped connectors and rigid lumps, the wide band gaps can exist with a compact spatial size. Moreover, the geometrical parameters are tunable in a large range. A maximum band gap of up to 63% is achievable. These salient merits outweigh the already published counterparts, enabling the proposed PnC strip to be a more promising candidate for engineering applications. Therefore, we are convinced that such a folding strategy of unit cells provides a practicable direction for the further structural design of PnC devices.

**Keywords:** phononic crystal strip, band gap, L-shaped connectors, folding strategy

## 1 Introduction

Phononic crystals (PnCs) that can alter the propagation of acoustic/elastic waves have attracted great attention [1–4]. The reported fascinating applications include waveguide [5–7], sound/vibration isolation and cloaking [8–10], acoustic subwavelength imaging [11], acoustic-optic coupling [12,13], etc. By now, abundant PnCs have been considered in the literature, with different mechanisms [14–16], 1D-to-3D periodicity [17,18], and various topologies [19,20]. Many effective methods have been introduced into the design of PnCs like popular topology optimization [19–21]. However, it is still a salient issue how to establish topologies to meet practical application demands. For example, PnCs can be designed as the supporting beams or the substrate of MEMS to alleviate or isolate elastic waves (MHz) induced by noise interference from the workplace or energy loss via supports and anchors [22,23]. Yet, the highly integrated MEMS imposed strict limits on the compatibility between band gaps and volume. On the other hand, because of technological constraints and costs when going to the microscale, robustness and machinability should be considered to avoid complex and impractical topologies.

One-dimensional (1D) PnC strips can save more space than their two-dimensional (2D) and three-dimensional (3D) counterparts, making them more suitable for low-space applications like MEMS. Moreover, because of their simplicity in both geometry structure and band structure, the 1D PnC strips are ideal carriers to verify new physical phenomena [24–26], new computational methods [27–29], and new materials [30,31]. Generally, according to the structural characteristics, 1D PnC strips can be divided into two types: holey PnC strips [24,32–38] and pillared PnC strips [39–47]. Comparatively, pillared PnC strips are more likely to induce wide band gaps and undoubtedly get more spotlight. Nevertheless, tall, heavy and hard pillars are always indispensable to provide strong local resonance for the generation of large band gaps. It has been revealed that a large band gap exists only when the ratio of the pillar height to substrate thickness reaches about 10 [39]. Even worse, the numerous pillars and layers of two different materials brought challenges in terms of space, fabrication, and stability. Referring to the holey PnC strips, nucleation of band gaps mainly relies on the Bragg scattering mechanism, which requires the geometry sizes to becommensurate with the wavelength. Thus, conventional holey PnC strips can hardly open large band gaps while keeping a small size, which greatly confines their applications. Up to now, many imaginative PnC strips have been proposed for cutting-edge physical research, but only a few can reconcile the theoretical properties and practicability.

In this paper, we propose an original convex-like 1D holey PnC strip. In a unit cell, four lumps are centrifugally connected by four L-shaped connectors. Unlike the conventional holey strips, the L-shaped connectors set up a folding topology, which elongates the wave propagation

* **Corresponding author: Shan Jiang,** State Key Laboratory of Digital Manufacturing Equipment and Technology, Huazhong University of Science and Technology, Wuhan, 430074, China, e-mail: jiangshan_hust@163.com
**Jun Jin, Hongping Hu:** Department of Mechanics, Huazhong University of Science and Technology, Wuhan, 430074, China

Open Access. © 2022 Jun Jin *et al.*, published by De Gruyter. This work is licensed under the Creative Commons Attribution 4.0 International License.

path but remains a compact geometry. Thorough research on band gaps has been conducted. The results are exactly what we expect: multiple wide band gaps exist in such a simple constitution while keeping a small size, with a large tunable range of geometrical parameters. All these traits are beneficial to improve feasibility, applicability, and reliability, making the proposed PnC strip a potential candidate for low-space applications. Finally, transmission spectra have been calculated to evaluate its ability in suppressing vibration.

The rest of this paper is arranged as follows. First, the geometrical constitution, theoretical basis, and main metrics are presented in Section 2. Second, the band structures and underlying mechanisms, the relationship between band gaps and geometrical parameters, and transmission spectra are discussed in Section 3. Finally, some conclusions are drawn in Section 4.

## 2 PnC strip model and theoretical basis

Here, we intended to reveal the essential traits of the proposed PnC, thus normalized parameters are applied throughout the theoretical analysis and numerical computation. With the benefits of normalization, the discussion is nearly geometry, material, and frequency agnostic instead of being confined to specific geometrical parameters, particular materials, and limited frequency ranges. Such treatment is widely used in theoretical analysis and numerical computation to capture the key issues. Furthermore, one can also conveniently determine geometrical and material parameters according to the actual requirements.

Figure 1 shows the sketch of the proposed holey PnC strip, in which a unit cell consists of four bulky lumps and four slender L-shaped connectors. The structure can be determined by four independent geometrical parameters ($b$, $c$, $d$ or other derivatives, and $h$). In the following discussion, these parameters are substituted by dimensionless variables, namely, be normalized against the lattice constant $a$ (set as 1 unit size).

The fundamental motion equation of elastic waves can be expressed by

$$\frac{\partial}{\partial x_j}\left(c_{ijkl}\frac{\partial u_k}{\partial x_l}\right) + \rho\omega^2 u_i = 0, \quad (i, j, k, l = 1, 2, 3), \tag{1}$$

where $c_{ijkl}$ is the elastic tensor, $x_j$ ($j = 1, 2, 3$) represent the coordinates $x$, $y$, and $z$, respectively, $u_i$ is the displacement, and $\omega$ denotes the circular frequency.

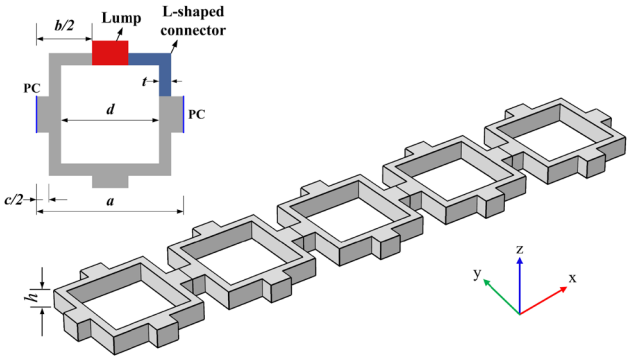


**Figure 1:** Sketch of the convex-like holey PnC strip with a unique folding topology provided by the constitution of bulky lumps and slender L-shaped connectors.

According to the Bloch theorem, the displacements must satisfy the following form:

$$\mathbf{u}(\mathbf{r}) = e^{-i\mathbf{k}\cdot\mathbf{r}}\tilde{\mathbf{u}}(\mathbf{r}), \tag{2}$$

where $\mathbf{k}$ is the Bloch wave vector, $\mathbf{r}$ is the position vector, and $\tilde{\mathbf{u}}$ is a periodical function with the same periodicity as the crystal lattice.

The involving calculations of band structures, essentially eigenvalues of partial differential equations, are implemented using commercial software COMSOL. The Bloch theorem is realized by applying Floquet periodic boundary conditions on the boundaries of a unit cell along with the corresponding directions. Dispersion relations can be obtained by sweeping the wave vector $\mathbf{k}$ along the edges of the first irreducible Brillouin zone. Since the topology includes four independent geometrical parameters, COMSOL modeling has been transformed into MATLAB script to perform the nested loops, significantly improving the computing efficiency.

The kinetic energetic ratio describing the polarization of elastic waves is defined as

$$e_i = \int_V u_i^2 dV \Big/ \int_V (u_x^2 + u_y^2 + u_z^2) dV, \quad i = x, y, z, \tag{3}$$

where $V$ is the volume. In the following discussion, this kind of information is helpful to understand the nucleation of the band gap. Moreover, it is also very important for the 1D PnC strip since it is sensitive to the polarization of elastic waves.

As the most important metric to evaluate the performance of PnCs, the band gaps are measured by a dimensionless parameter, *viz.*, the ratio between the width and center frequency. BG% = $2(f_{top} - f_{bot})/(f_{top} + f_{bot})$, where $f_{bot}$ and $f_{top}$ are the edges of band gaps. Generally, a higher BG% value is preferable.

# 3 Results and discussion

## 3.1 Band structures

Figure 2 shows the band structure of the proposed PnC strip with geometrical parameters ($b/a$, $c/a$, $d/a$, $h/a$) = (0.82, 0.22, 0.65, 0.15), in which the normalized wavenumber ($ka/2\pi$) and normalized frequency ($\omega a/2\pi c_t$) are applied to abstract the dispersion relations. As the definition stated, the band structure is material and lattice constant $a$ agnostic, and only depends on the combination of ($b/a$, $c/a$, $d/a$, $h/a$). The chosen material for numerical examples in this work is single crystal silicon. Its material parameters are the mass density $\rho$ = 2320 kg·m$^{-3}$, the elastic constants $c_{11}$ = 165.7 GPa,

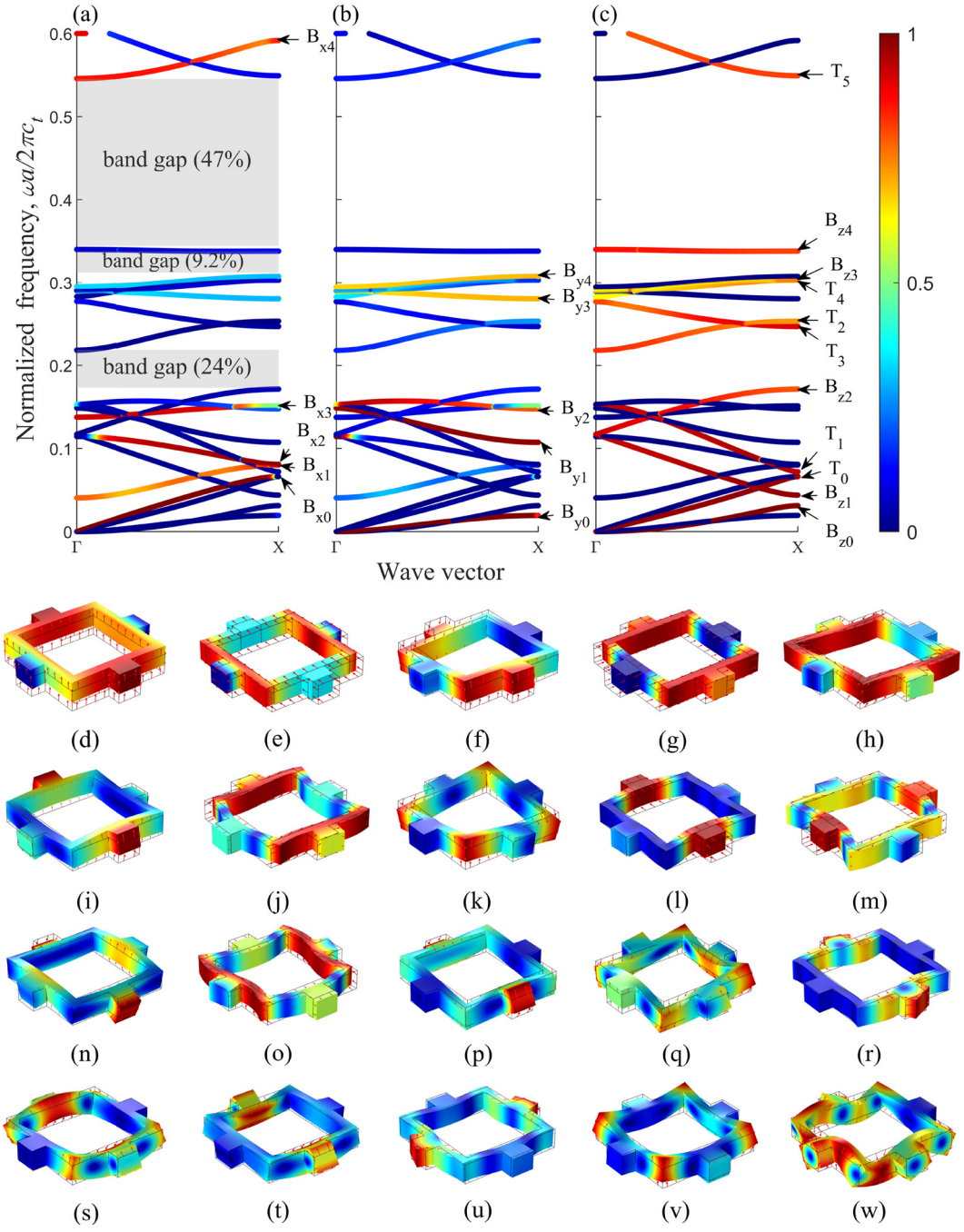


**Figure 2:** (a) Band structure of the convex-like holey PnC strip with geometrical parameters ($b/a$, $c/a$, $d/a$, $h/a$) = (0.82, 0.22, 0.65, 0.15). Color denotes the kinetic energetic ratio $e_i$ ($i = x, y, z$), describing the polarization of elastic waves. (a–c) correspond to $x$, $y$, and $z$ polarizations respectively. (d–w) Identified eigenmodes corresponding to the bands in the band structure.

$c_{12}$ = 64.1 GPa and $c_{44}$ = 79.6 GPa, and transverse and longitudinal speeds $c_t$ = 5,840 m·s$^{-1}$ and $c_l$ = 8,433 m·s$^{-1}$, respectively. The $y$ and $x$ coordinates of the strip are consistent with the [010] direction of a (100)-oriented silicon wafer.

The band structure has been repeated three times with different kinetic energetic ratios $e_i$ ($i = x, y, z$), which is embodied by color. In virtue of such information, one can easily distinguish the polarization belonging of each band. At a glance, three band gaps are visible, whose normalized frequency spans are 0.173–0.220, 0.310–0.340, and 0.342–0.550, corresponding to BG% of 24%, 9.2%, and 47%, respectively. The latter two band gaps are separated by a quasi-flat band, and its group velocity is close to zero.

To understand the nucleating mechanisms of band gaps, the eigenmodes of the first 20 bands at $ka/2\pi = 0.25$ are also demonstrated in Figure 2 (d–w). Γ and X at the ends are equal to 0 and 0.5, respectively. Four basic bands are starting from $\omega = 0$ in the 1D PnC strip, which can be further classified as four different types: the $x$-bending mode ($B_{x0}$), $y$-bending mode ($B_{y0}$), $z$-bending mode ($B_{z0}$), and torsional mode ($T_0$). The other bands are higher-order derivatives of these four basic modes. For simplifying the discussion, these modes can be further divided into in-plane modes (including $B_x$- and $B_y$-modes) and out-of-plane modes (including $B_z$- and T-modes). Each band in the band structure is labeled. By comparing the boundary eigenmodes of band gaps, it can be concluded that the mismatch of the displacement distribution between the consecutive bands forms a band gap. A steeper mismatch is conducive to inducing a larger band gap.

Basically, band gaps of the holey PnCs are mainly induced by the Bragg scattering mechanism, which stipulates the proportionality between the geometrical size and wavelength. In other words, it is challenging to open a large band gap with a small size. Unlike the conventional holey structures, the unique folding topology in this work enables the elongation of propagating path while remaining a limited size. It is effective to circumvent the limitation of Bragg band gaps on geometrical dimensions. On the other hand, in the eigenmodes, especially in the bending modes, the lumps act as rigid bodies while L-shaped connectors act as deformable bodies. The big difference in bending stiffness can also sustain the local resonance mechanism. Specifically, the large mismatch of localized vibration energy in distinct resonant modes can also enhance the reflectivity of waves. Based on the above analysis, we deduce that the nucleation of the multiple wide band gaps roots in the combination of Bragg scattering mechanism and local resonance mechanism.

L-Shaped connectors play an important role in the high-performance band gaps. As for the mechanical behaviors of L-shaped connectors, refs [48,49] give an in-depth theoretical analysis. In a nutshell, the behaviors of L-shaped structures include axial motion, in-plane bending, out-of-plane bending, and torsional motion. Both theoretical equations and numerical analysis confirm that these motions can be well decoupled into in-plane and out-of-plane motions, which is in good consistency with the classification of eigenmodes in Figure 2. For the in-plane modes ($B_x$- and $B_y$-modes), the motion of the L-shaped connectors is a coupling of axial extension and in-plane bending. As for the out-of-plane modes ($B_z$- and T-modes), the motion of the L-shaped connectors is a coupling of out-of-plane bending and torsional motion.

## 3.2 Comparison with counterparts

To illustrate the advantages of the proposed PnC strip, a comparison of the band structures with three previously published strips is shown in Figure 3, including I-like strip [32], improved I-like strip [33], and cross-like strip [34]. The chosen material and computational method are identical. Color uniformly represents the kinetic energy ratio $e_z$. By contrast, Figure 3 reveals some interesting regularities. First, although Figure 4(a) and (b) are similar I-like strips, the band gap of improved I-like strip from hexagonal lattice is much wider and lower than the standard counterpart from a square lattice. Second, the strips in Figure 3(c) and (d) have much more additional free boundaries than those in Figure 3(a) and (b), which is helpful to arouse the low-frequency wave modes. Third, the thicknesses in Figure 3(c) and (d) are only $h/a$ = 0.2 and $h/a$ = 0.15, whereas much larger $h/a$ = 0.75 and $h/a$ = 0.43 in Figure 3(a) and (b). Finally, Figure 3(d) has advantages of multiple broad band gaps, lower frequency band gap, and a much smaller size than the previous PnC strips.

## 3.3 Geometrical optimization for largest band gaps

Then, geometrical optimization aiming to probe the largest value of BG% has been conducted. In general, the topology involving multiple geometrical parameters is preferable, which can offer more possibilities to tune band gaps. In the proposed convex-like PnC strip, four independent parameters need to be considered. Here, we use a combination of $b$, $c$, $w$, and $h$, where $w = a - 2t$. The reason to choose $w$ rather than others is that we want to

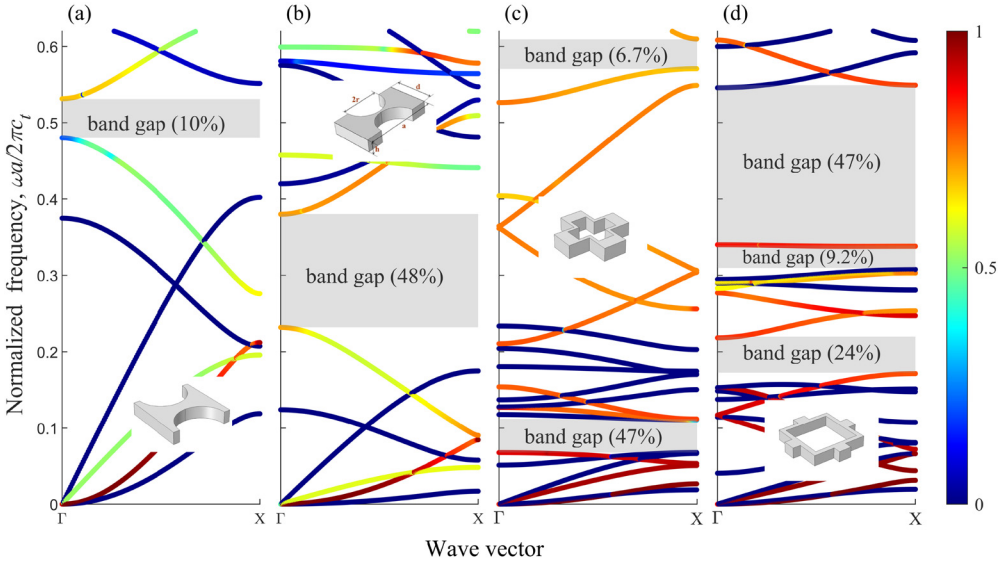


**Figure 3:** Comparison on band structures of (a) I-like strip with ($r/a$, $h/a$) = (0.36, 0.75), (b) improved I-like strip with ($a/d$, $r/d$, $h/d$) = ($3^1/^2$, 0.45, 0.75), (c) cross-like strip with ($b/a$, $c/a$, $d/a$, $h/a$) = (0.625, 0.25, 0.65, 0.2), and (d) the proposed convex-like PnC strip with ($b/a$, $c/a$, $d/a$, $h/a$) = (0.82, 0.22, 0.65, 0.15).

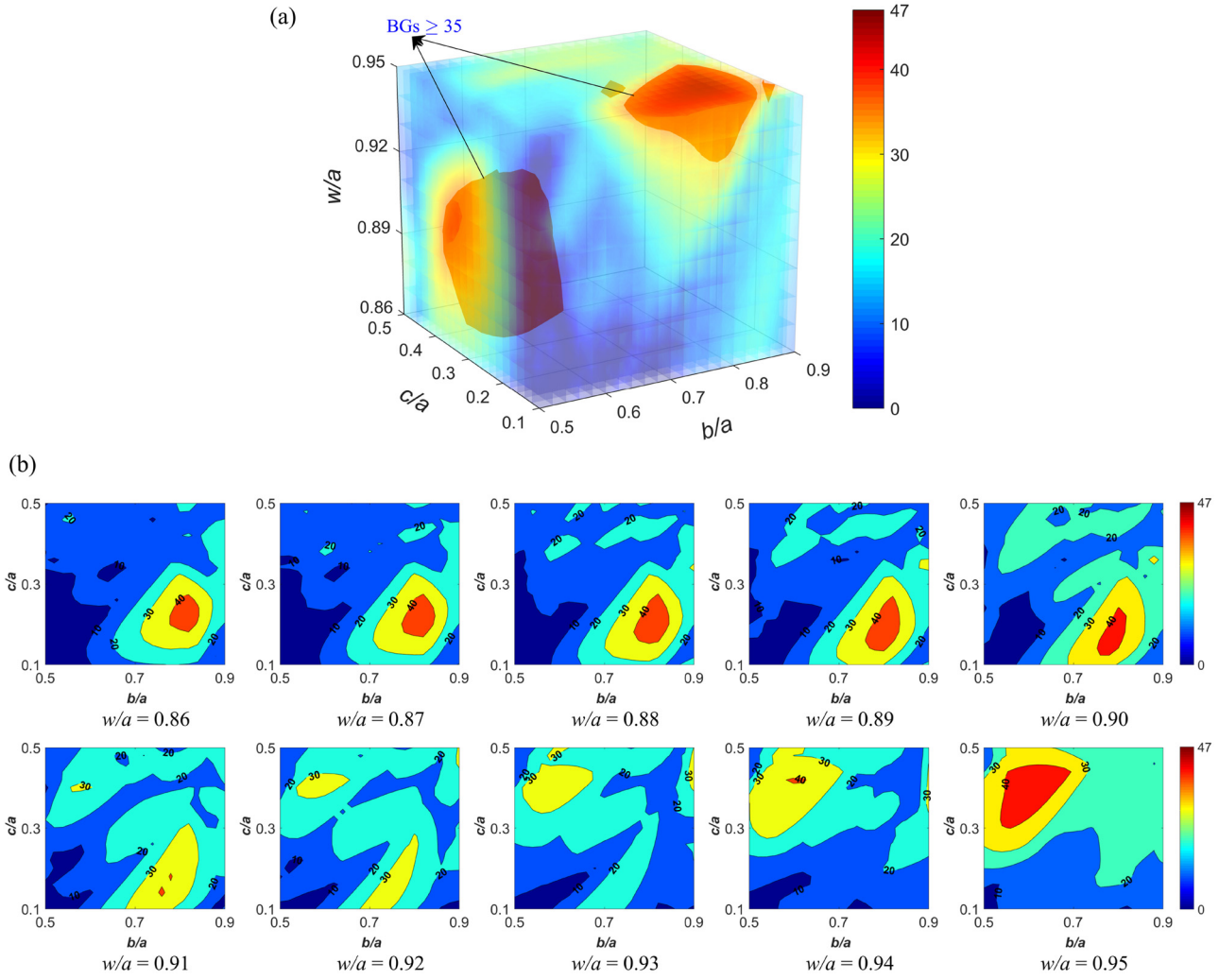


**Figure 4:** The combined effect of in-plane geometrical parameters ($b/a$, $c/a$, and $w/a$) on band gaps, where BG% is represented by color. Out-of-plane geometrical parameter $h/a$ = 0.15. (b) Ten slices extracted from (a), each slice demonstrates the influence of $b/a$ and $c/a$ on the band gaps for a given $w/a$.

vary the crucial width of L-shaped connectors $t$ gradually smaller and make this variation accord with the positive direction of the $z$-axis (gradually larger). Moreover, these four geometrical parameters are further categorized as in-plane ($b$, $c$, and $w$) and out-of-plane parameters (thickness $h$). The out-of-plane parameter can only influence the out-of-plane modes ($B_z$- and T-modes), while the in-plane parameters can affect all modes significantly. As a result, the best strategy to make the band gaps as wide as possible is to prevent the out-of-plane modes from splitting the band gaps or minimize the effect if the interference is inevitable. Specifically, the effect of the in-plane parameters ($b$, $c$, and $w$) is considered first by the nested loop to adjust the overall band structure, and then the out-of-plane parameter $h$ is varied to relocate the special bands.

The joint effect of $b/a$, $c/a$, and $w/a$ on band gaps are integrated into Figure 4(a), in which BG% is shown by color. The out-of-plane parameter $h/a$ fixes at 0.15 during the iterative calculation. One can easily have an insight into the influence of each parameter and then their optimal combinations. Furthermore, ten slices along the parameter $w/a$ extracted from Figure 4(a) are shown in Figure 4(b), each slice demonstrates the dependence of

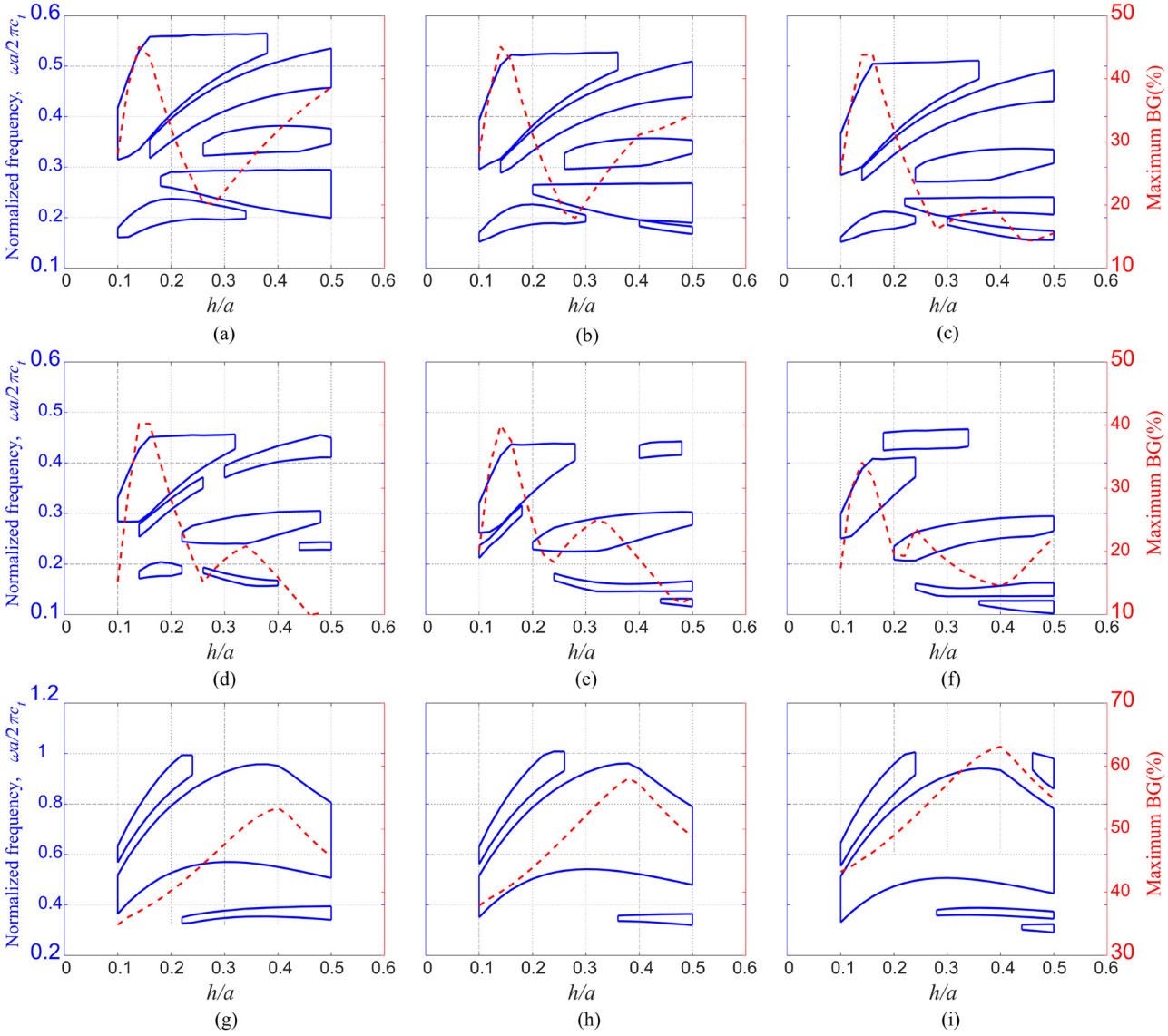


**Figure 5:** Variation of band gaps versus the out-of-plane geometrical parameter $h/a$, where $w/a$ varies from 0.87 to 0.95. $b/a$ and $c/a$ are optimum values corresponding to each $w/a$ attained from Figure 4. The blue left $y$-axis and red right $y$-axis represent the position of band gaps and the corresponding maximum BG%, respectively. (a) $w/a$ = 0.87, (b) $w/a$ = 0.88, (c) $w/a$ = 0.89, (d) $w/a$ = 0.90, (e) $w/a$ = 0.91, (f) $w/a$ = 0.92, (g) $w/a$ = 0.93, (h) $w/a$ = 0.94, and (i) $w/a$ = 0.95.

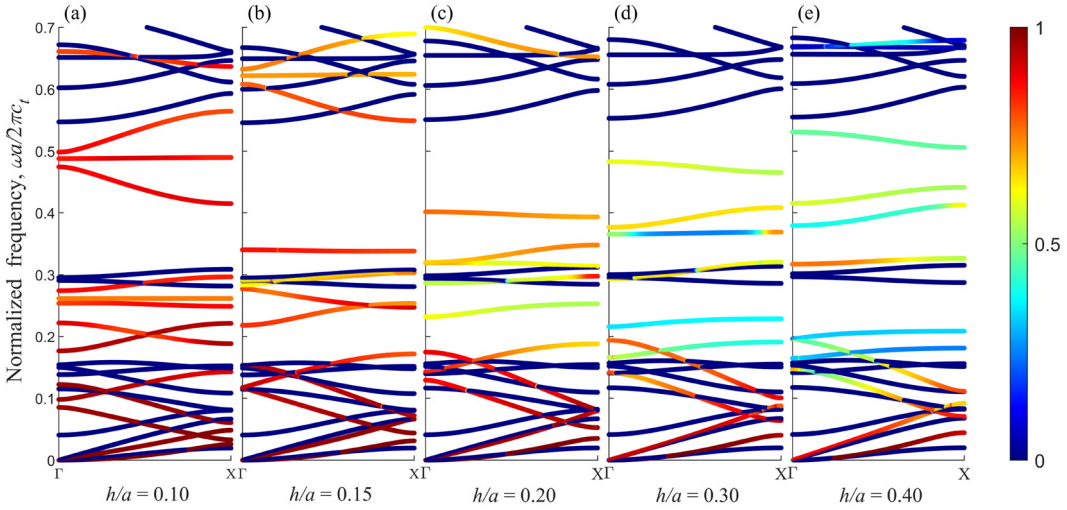


**Figure 6:** Effect of $h/a$ on the band structure with $(b/a, c/a, d/a) = (0.82, 0.22, 0.65)$. Color denotes the kinetic energy ratio $e_z$. (a) $h/a = 0.10$; (b) $h/a = 0.15$; (c) $h/a = 0.20$; (d) $h/a = 0.30$; and (e) $h/a = 0.40$.

**Table 1:** The effect of $t/a$ on the largest BG% and the supporting parameters

| $t/a$ | $f_{top}$ | $f_{bot}$ | BG% | $(b/a, c/a, d/a)$ | $h/a$ |
|---|---|---|---|---|---|
| 0.070 | 0.566 | 0.356 | 45.49 | (0.82, 0.22, 0.64) | 0.15 |
| 0.065 | 0.550 | 0.342 | 46.63 | (0.82, 0.22, 0.65) | 0.15 |
| 0.060 | 0.522 | 0.325 | 46.37 | (0.82, 0.20, 0.68) | 0.15 |
| 0.055 | 0.492 | 0.311 | 44.93 | (0.80, 0.18, 0.71) | 0.15 |
| 0.050 | 0.449 | 0.288 | 43.47 | (0.78, 0.14, 0.76) | 0.15 |
| 0.045 | 0.434 | 0.286 | 41.24 | (0.76, 0.14, 0.77) | 0.15 |
| 0.040 | 0.286 | 0.407 | 35,17 | (0.72, 0.12, 0.80) | 0.15 |
| 0.035 | 0.550 | 0.951 | 53.38 | (0.60, 0.42, 0.51) | 0.40 |
| 0.030 | 0.528 | 0.961 | 58.08 | (0.60, 0.42, 0.52) | 0.38 |
| 0.025 | 0.486 | 0.934 | 63.10 | (0.62, 0.42, 0.53) | 0.40 |

band gaps on $b/a$ and $c/a$ for a given $w/a$, by which one can understand the variation tendency quantitatively and intuitively. From Figure 4(a), the first and perhaps most remarkable feature is that wide band gaps exist with a broad tunable range of parameters. Two big red kernels denoting the broad band gaps (BG% ≥ 35%) can be reached in two large regions. More specifically in Figure 4(b), with the increase of $w/a$ from 0.86 to 0.95, the BG% of the first kernel peaks at intermediate values and then decreases gradually until vanishing. However, for another one, kernel forms and spreads, and BG% increases accordingly with the increase of $w/a$. The widest band gap obtained has BG% = 47%.

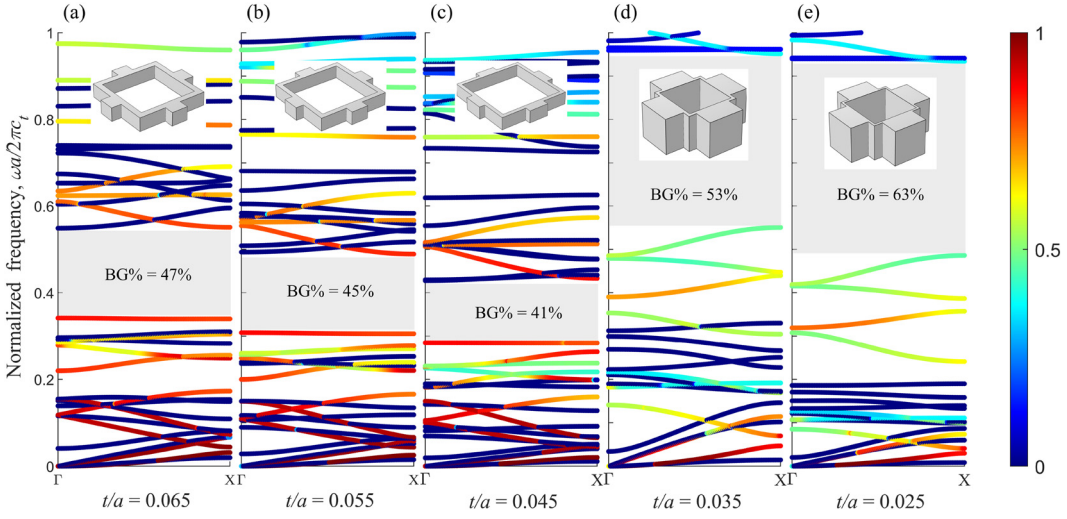


**Figure 7:** Band structures of $t/a$ = (a) 0.065, (b) 0.055, (c) 0.045, (d) 0.035, and (e) 0.025. Color denotes the kinetic energy ratio $e_z$.

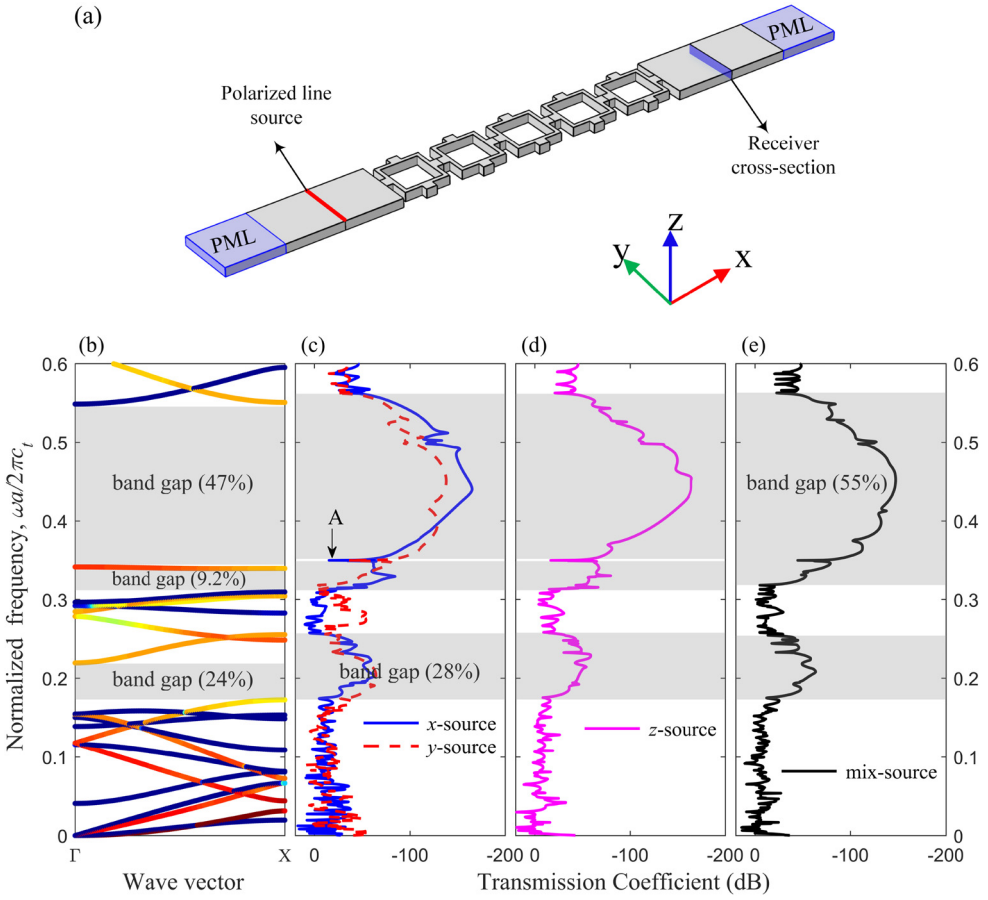


**Figure 8:** (a) Sketch of the setup for the transmission spectra. (b) Band structure. (c)–(e) Achieved transmission spectra under different excitations.

Next, Figure 5 gives the effect of the out-of-plane parameter $h/a$ on band gaps, under different $w/a$ values. The blue left $y$-axis shows the position of band gaps, and the red right $y$-axis is the maximum BG%. While $w/a$ varies from 0.87 to 0.95, the chosen $b/a$ and $c/a$ are optimum values corresponding to each $w/a$ attained from Figure 4. It should be mentioned that the ranges of vertical axes are different. The variation trends of band gaps in Figure 5 echo the features manifested by Figure 4. Obviously, the band structure has a sudden change when $w/a$ varies from 0.92 to 0.93, which can be attributed to the different nucleating ways of band gaps. It corresponds to the two red kernels in Figure 4. The optimum $h/a$ remains constant at 0.15 when $w/a \leq 0.92$. However, the optimum $h/a$ moves to about 0.4 when $w/a > 0.92$.

As a supplement, to present the effect of $h/a$ more vividly, the variation of band structure has also been directly illustrated in Figure 6. Evidently, when the value of $h/a \leq 0.4$, the thickness $h$ just affects $B_z$-modes and T-modes. It further verifies the earlier discussion. The reason for this is because the parameter $h$ has a monotonic relationship with both the $z$-bending stiffness and torsion stiffness, but is tangential to the in-plane bending stiffness.

The combination of Figures 4 and 5 provides the maximum of BG% and the corresponding optimal parameters. In other words, a thorough investigation based on geometrical optimization has been implemented. Among these geometrical parameters, the width of L-shaped connectors $t$ is worth special attention since it is the smallest feature size limiting the fabrication and it is crucial on the lump-connector system. Table 1 summarizes the effect of $t/a$ on the largest BG% and the supporting parameters. The largest BG% can be obtained when $t/a$ is close to the limit, but considering the possible manufacturing inaccuracy and fabrication limitations, it is better not to keep the $t/a$ too small.

Figure 7 compares the band structures of $t/a = 0.065$, 0.055, 0.045, 0.035, and 0.025. With the decrease of $t/a$, the difference of bending stiffness between the deformable L-shaped connectors and rigid lumps increases, which results in the restructuring of band structures

and the new optimal combination of geometry parameters. In Figure 7(e), the mismatch of mechanical properties of L-shaped connectors and rigid lumps reaches a very extreme level. The in-plane bands (blue color) have been greatly suppressed in low frequencies due to the heavy lumps.

### 3.4 Transmission coefficient

The transmission coefficient is another important consideration, which can corroborate the band gaps achieved by the infinite theoretical model and characterize the attenuation of a finite periodic structure on elastic waves. The schematic setting for the simulation of transmission spectra is shown in Figure 8(a). The polarized line sources include *x*-, *y*-, *z*-, and mixed polarization, which is very useful for simulating practical applications. The cross-sectional probe is deployed behind five periods. Perfectly match layers (PML) have been arranged at the ends to alleviate the reflections of outgoing waves [50].

The calculated transmission spectra for line sources with different directions are presented in Figure 8(c)–(e), where (c) for *x*- and *y*-polarized displacements, (d) for *z*-polarized displacement, and (e) for a mix-polarized displacement. Compared to Figure 8(b), the attenuating ranges match well with the band gaps. However, several points need to be highlighted. First, a peak "A" supposed to be nonexistent appears at $\omega a/2\pi c_t \approx 0.35$ in Figure 8(c). It corresponds to the *z*-directional modal shape $B_{z4}$ excited by the *x*-polarized line source. Second, there is a subtle discrepancy between the band structure and transmission spectra on the upper edge frequencies of band gaps. It might be because some modes are deaf modes that are immune to the applied polarized line sources.

## 4 Conclusion

In this work, we proposed an original convex-like 1D holey PnC strip. Its potential application background might be the control of the propagation of acoustic or elastic waves in high-integration devices like MEMS. A comprehensive investigation of band gaps based on the geometrical optimization has been performed by using the finite element method. The production mechanisms are analyzed in virtue of the energy method. Compared with the conventional counterparts, the superiority lies in its simplicity, smaller size, and multiple large band gaps that can exist over a wide range of parameters. The unique folding topology constituted by L-shaped connectors provides a practicable solution for the limitations of conventional PnCs. We are convinced that these topics are conducive to further structural designs and novel applications of PnC devices.

**Funding information:** This work was supported by the National Natural Science Foundation of China (Grant Nos. 52105575 and 11872186), the China Postdoctoral Science Foundation (Grant No. 2020M672331), and Fundamental Research Funds for the Central Universities (HUST: 2016JCTD114).

**Author contributions:** Shan Jiang, Jun Jin and Hongping Hu conceived the idea and designed the research. Shan Jiang and Jun jin wrote the manuscript. Hongping Hu revised the manuscript.

**Conflict of interest:** The authors state no conflict of interest.

**Data availability statement:** All data used to support the findings of this study are included within the article.

## References

[1] Hussein, M. I., M. J. Leamy, and M. Ruzzene. Dynamics of phononic materials and structures: Historical origins, recent progress, and future outlook. *Applied Mechanics Reviews*, Vol. 66, No. 4, 2014, id. 040802.

[2] Laude, V. *Phononic crystals: artificial crystals for sonic, acoustic, and elastic waves*, Walter de Gruyter GmbH & Co KG, Berlin, Germany, 2015.

[3] Wang, Y., Y. Wang, B. Wu, W. Chen, and Y. Wang. Tunable and active phononic crystals and metamaterials. *Applied Mechanics Reviews*, Vol. 72, No. 4, 2020, id. 040801.

[4] Lim, C. W. From Photonic Crystals to seismic metamaterials: a review via phononic crystals and acoustic metamaterials. *Archives Computational Methods Engineering*, Vol. 29, 2022, pp. 1137–1198.

[5] Jin, Y., N. Fernez, Y. Pennec, B. Bonello, R. P. Moiseyenko, S. Hémon, et al. Tunable waveguide and cavity in a phononic crystal plate by controlling whispering-gallery modes in hollow pillars. *Physical Review B*, Vol. 93, No. 5, 2016, id. 054109.

[6] Kurosu, M., D. Hatanaka, K. Onomitsu, and H. Yamaguchi. On-chip temporal focusing of elastic waves in a phononic crystal waveguide. *Nature communications*, Vol. 9, No. 1, 2018, id. 1331.

[7] Ghasemi Baboly, M., C. M. Reinke, B. A. Griffin, I. El-Kady, and Z. Leseman. Acoustic waveguiding in a silicon carbide

phononic crystals at microwave frequencies. *Applied Physics Letters*, Vol. 112, No. 10, 2018, id. 103504.
[8] Cummer, S. A., J. Christensen, and A. Alù. Controlling sound with acoustic metamaterials. *Nature Reviews Materials*, Vol. 1, No. 3, 2016, id. 16001.
[9] Jiang, S., H. Chen, L. X. Dai, H. P. Hu, and V. Laude. Multiple low-frequency broad band gaps generated by a phononic crystal of periodic circular cavity sandwich plates. *Composite Structures*, Vol. 176, 2017, pp. 294–303.
[10] Ning, L., Y. Wang, and Y. Wang. Active control cloak of the elastic wave metamaterial. *International Journal of Solids & Structures*, Vol. 202, 2020, pp. 126–135.
[11] Zhu, J., J. Christensen, J. Jung, L. Martin-Moreno, X. Yin, L. Fok, et al. A holey-structured metamaterial for acoustic deep-subwavelength imaging. *Nature Physics*, Vol. 7, No. 1, 2011, pp. 52–55.
[12] Pennec, Y., V. Laude, N. Papanikolaou, B. Djafari-Rouhani, M. Oudich, S. El Jallal, et al. Modeling light-sound interaction in nanoscale cavities and waveguides. *Nanophotonics*, Vol. 3, No. 6, 2014, pp. 413–440.
[13] Jin, J., S. Jiang, H. Hu, L. Zhan, X. Wang, and V. Laude. Acousto-optic cavity coupling in 2D phoxonic crystal with combined convex and concave holes. *Journal of Applied Physics*, Vol. 130, No. 12, 2021, id. 123104.
[14] Liu, Z. Y., X. X. Zhang, Y. W. Mao, Y. Zhu, Z. Y. Yang, C. T. Chan, et al. Locally resonant sonic materials. *Science*, Vol. 289, No. 5485, 2000, pp. 1734–1736.
[15] Lee, T. and H. Iizuka. Bragg scattering based acoustic topological transition controlled by local resonance. *Physical Review B*, Vol. 99, No. 6, 2019, id. 064305.
[16] Krushynska, A. O., M. Miniaci, F. Bosia, and N. M. J. E. M. L. Pugno. Coupling local resonance with Bragg band gaps in single-phase mechanical metamaterials. *Extreme Mechanics Letters*, Vol. 12, 2017, pp. 30–36.
[17] D'Alessandro, L., E. Belloni, R. Ardito, A. Corigliano, and F. Braghin. Modeling and experimental verification of an ultra-wide bandgap in 3D phononic crystal. *Applied Physics Letters*, Vol. 109, No. 22, 2016, id. 221907.
[18] Li, W., F. Meng, Y. Fan Li, and X. Huang. Topological design of 3D phononic crystals for ultra-wide omnidirectional bandgaps. *Structural and Multidisciplinary Optimization*, Vol. 60, No. 6, 2019, pp. 2405–2415.
[19] Dong, H. W., Y. S. Wang, and C. Z. Zhang. Topology optimization of chiral phoxonic crystals with simultaneously large phononic and photonic bandgaps. *IEEE Photonics Journal*, Vol. 9, No. 2, 2017, pp. 1–16.
[20] Li, W., F. Meng, Y. Chen, Y. F. Li, and X. J. Huang. Topology optimization of photonic and phononic crystals and metamaterials: a review. *Advanced Theory and Simulations*, Vol. 2, No. 7, 2019, id. 1900017.
[21] Dong, H. W., Y. S. Wang, T. X. Ma, and X. X. Su. Topology optimization of simultaneous photonic and phononic bandgaps and highly effective phoxonic cavity. *JOSA B*, Vol. 31, No. 12, 2014, pp. 2946–2955.
[22] Bao, F., X. Wu, X. Zhou, Q. Wu, X. Zhang, and J. Bao. Spider web-like phononic crystals for piezoelectric MEMS resonators to reduce acoustic energy dissipation. *Micromachines*, Vol. 10, No. 9, 2019, id. 626.
[23] Workie, T. B., T. Wu, J.-F. Bao, and K.-Y. Hashimoto. Design for high-quality factor of piezoelectric-on-silicon MEMS resonators using resonant plate shape and phononic crystals. *Japanese Journal of Applied Physics*, Vol. 60, No. SD, 2021, id. SDDA03.
[24] Zhang, Z., Y. Cheng, X. Liu, and J. Christensen. Subwavelength multiple topological interface states in one-dimensional labyrinthine acoustic metamaterials. *Physical Review B*, Vol. 99, No. 22, 2019, id. 224104.
[25] Zhou, W. and C. J. I. J. O. M. S. Lim. Topological edge modeling and localization of protected interface modes in 1D phononic crystals for longitudinal and bending elastic waves. *International Journal of Mechanical Sciences*, Vol. 159, 2019, pp. 359–372.
[26] Arrangoiz-Arriola, P., E. A. Wollack, M. Pechal, J. D. Witmer, J. T. Hill, and A. H. Safavi-Naeini. Coupling a superconducting quantum circuit to a phononic crystal defect cavity. *Physical Review X*, Vol. 8, No. 3, 2018, id. 031007.
[27] Qian, D. and Z. J. P. L. A. Shi. Using PWE/FE method to calculate the band structures of the semi-infinite beam-like PCs: Periodic in z-direction and finite in x–y plane. *Physics Letters A*, Vol. 381, No. 17, 2017, pp. 1516–1524.
[28] Qian, D. and Z. Shi. Using PWE/FE Method to Calculate the Band Structures of the Semi-Infinite PCs: Periodic in xy Plane and Finite in z–direction. *Archives of Acoustics*, Vol. 42, 2017.
[29] Cheng, J., G. Wang, and Y. J. E. A. W. B. E. Wu. A hybrid plane wave expansion/edge-based smoothed finite element method for band structures simulation of semi-infinite beam-like phononic crystals. *Engineering Analysis with Boundary Elements*, Vol. 130, 2021, pp. 176–185.
[30] Aly, A. H., A. Nagaty, and A. Mehaney. One-dimensional phononic crystals that incorporate a defective piezoelectric/piezomagnetic as a new sensor. *The European Physical Journal B*, Vol. 91, No. 10, 2018, pp. 1–5.
[31] Lou, J., L. He, J. Yang, S. Kitipornchai, and H. J. A. A. Wu. Wave propagation in viscoelastic phononic crystal rods with internal resonators. *Applied Acoustics*, Vol. 141, 2018, pp. 382–392.
[32] Hsu, F. C., C. I. Lee, J. C. Hsu, T. C. Huang, C. H. Wang, and P. Chang. Acoustic band gaps in phononic crystal strip waveguides. *Applied Physics Letters*, Vol. 96, No. 5, 2010, id. 051902.
[33] Feng, D., D. H. Xu, G. Q. Wu, B. Xiong, and Y. L. Wang. Extending of band gaps in silicon based one-dimensional phononic crystal strips. *Applied Physics Letters*, Vol. 103, No. 15, 2013, id. 151906.
[34] Jiang, S., H. P. Hu, and V. Laude. Low-frequency band gap in cross-like holey phononic crystal strip. *Journal of Physics D: Applied Physics*, Vol. 51, No. 4, 2018, id. 045601.
[35] Li, C. S., D. Huang, J. R. Guo, and J. J. Nie. Engineering of band gap and cavity mode in phononic crystal strip waveguides. *Physics Letters A*, Vol. 377, No. 38, 2013, pp. 2633–2637.
[36] Ha, T. D. Boosted anchor quality factor of a thin-film aluminum nitride-on-silicon length extensional mode MEMS resonator using phononic crystal strip. *Applied Physics A*, Vol. 127, No. 10, 2021, pp. 1–9.
[37] Lim, C., J. T. Li, and Z. J. E. M. L. Zhao. Lightweight architected lattice phononic crystals with broadband and multiband vibration mitigation characteristics. *Extreme Mechanics Letters*, Vol. 41, 2020, id. 100994.
[38] Ampatzidis, T. and D. Chronopoulos. Mid-frequency band gap performance of sandwich composites with unconventional core geometries. *Composite Structures*, Vol. 222, 2019, id. 110914.

[39] Wu, T. C., T. T. Wu, and J. C. Hsu. Waveguiding and frequency selection of Lamb waves in a plate with a periodic stubbed surface. *Physical Review B*, Vol. 79, No. 10, 2009, id. 104306.
[40] Bilal, O. R. and M. I. Hussein. Trampoline metamaterial: Local resonance enhancement by springboards. *Applied Physics Letters*, Vol. 103, No. 11, 2013, id. 111901.
[41] Ma, C. Y., J. W. Guo, and Y. F. Liu. Extending and lowing band gaps in one-dimensional phononic crystal strip with pillars and holes. *Journal of Physics and Chemistry of Solids*, Vol. 87, 2015, pp. 95–103.
[42] Coffy, E., T. Lavergne, M. Addouche, S. Euphrasie, P. Vairac, and A. Khelif. Ultra-wide acoustic band gaps in pillar-based phononic crystal strips. *Journal of Applied Physics*, Vol. 118, No. 21, 2015, id. 214902.
[43] Feng, D., W. L. Jiang, D. H. Xu, B. Xiong, and Y. L. Wang. Micro-silicon phononic crystal with locally resonant theory. *Applied Physics Letters*, Vol. 110, No. 17, 2017, id. 171902.
[44] Huang, Y., J. Li, W. Chen, and R. Bao. Tunable bandgaps in soft phononic plates with spring-mass-like resonators. *International Journal of Mechanical Sciences*, Vol. 151, 2019, pp. 300–313.
[45] Jin, Y., Y. Pennec, B. Bonello, H. Honarvar, L. Dobrzynski, B. Djafari-Rouhani, et al. Physics of surface vibrational resonances: pillared phononic crystals, metamaterials, and metasurfaces. *Reports on Progress in Physics*, Vol. 84, No. 8, 2021, id. 086502.
[46] Fan, L., Y. He, X. Chen, and X. Zhao. Acoustic energy harvesting based on the topological interface mode of 1D phononic crystal tube. *Applied Physics Express*, Vol. 13, No. 1, 2019, id. 017004.
[47] Kim, I., S. Iwamoto, and Y. J. A. P. E. Arakawa. Topologically protected elastic waves in one-dimensional phononic crystals of continuous media. *Applied Physics Express*, Vol. 11, No. 1, 2017, id. 017201.
[48] Georgiades, F., J. Warminski, and M. P. Cartmell. Linear modal analysis of L-shaped beam structures. *Mechanical Systems and Signal Processing*, Vol. 38, No. 2, 2013, pp. 312–332.
[49] Georgiades, F., J. Warminski, and M. P. Cartmell. Towards linear modal analysis for an L-shaped beam: Equations of motion. *Mechanics Research Communications*, Vol. 47, 2013, pp. 50–60.
[50] Diatta, A., M. Kadic, M. Wegener, and S. Guenneau. Scattering problems in elastodynamics. *Physical Review B*, Vol. 94, No. 10, 2016, id. 100105.